Supplementary Information for

A biofuel cell of (methyl violet/AuNPs)$_{25}$/FTO photoanode and bilirubin oxidase/CuCo$_2$O$_4$ bio-photocathode inspired by the photoelectrochemistry activities of fluorescent materials/molecules

Chenglong Sun[a,b], Xingyu Zeng[a], Mingjian Chen[a], Yun Du[a,c], Yueyi Peng[a], Qingji Xie*[a]

[a.] Key Laboratory of Chemical Biology & Traditional Chinese Medicine Research (Ministry of Education of China), College of Chemistry and Chemical Engineering, Hunan Normal University, Changsha 410081, China.

[b.] School of Materials Science and Engineering, Peking University, Beijing 100871, China.

[c.] Changsha Center for Diseases Prevention and Control, Changsha 410004, China.

† E-mail: xieqj@hunnu.edu.cn.

The charge transfer by redox chemistry and electricity generation in photocatalysis and PEC

Obviously, the photocatalysis and PEC performance is determined by the charge transfer performance. The charge transfer by redox chemistry and electricity generation in photocatalysis and PEC is explained below.

(1) In both photocatalysis and PEC, the exposed CB electrons as reductants can react with solution-state chemical oxidants at the semiconductor|solution interface, and the exposed VB holes as oxidants can simultaneously react with solution-state chemical reductants also at the semiconductor|solution interface.

(2) In PEC, the CB electrons and VB holes can not only directly initiate such interfacial redox twin-reactions at the semiconductor|solution interface, but also flow to the external circuit for both generating electricity and indirectly initiating a single interfacial reduction or oxidation reaction at the PEC-inactive counter electrode.

Frontier molecular orbital theory of fluorescent molecules

For UV-Vis light-absorbing molecules at room temperature, light irradiation can drive the electronic energy level transition, namely, the ground-state electrons on the highest occupied molecular orbital (HOMO, similar to the VB for semiconductors) can enter on the lowest unoccupied molecular orbital (LUMO, similar to the CB for semiconductors) to become the photo-excited electrons after light irradiation. The photo-excited LUMO electrons of fluorescence-inactive molecules can release the energy only by the relatively fast nonradiative-recombination (heat-release) such as vibrational relaxation ($10^{-14}\sim10^{-12}$ s) and internal conversion ($10^{-11}\sim10^{-9}$ s)[1]. In contrast, the photo-excited LUMO electrons of fluorescence-active molecules have the relatively long lifetime ($10^{-10}\sim10^{-7}$ s)[2].

Materials and apparatus

FTO (model P003, film resistance < 15 Ω cm^{-2}) was purchased from Zhuhai Kaivo Optoelectronics Technology Co., Ltd. (Zhuhai, China). BOD (5 U/mg) was purchased from Shanghai Aladdin Biochemical Technology Co., Ltd. (Shanghai, China). Tetrachloroaurate trihydrate (HAuCl$_4$·3H$_2$O) and AA were supplied from Sigma-Aldrich. Thioglycolic acid (TGA), KCl, CdCl$_2$·2.5H$_2$O, NaOH, Na$_2$S·9H$_2$O, yttrium chloride (YCl$_3$), ytterbium chloride (YbCl$_3$·6H$_2$O), thulium chloride (TmCl$_3$), ammonium fluoride (NH$_4$F), oleic acid (OA), Rh6G, pyrrole, sodium dodecylbenzene sulfonate (SDBS), Na$_2$SO$_3$, Na$_2$SO$_4$, H$_2$SO$_4$, rose red B (RhB), NR, MV (C$_{24}$H$_{27}$N$_3$·HCl, the structural formula of MV is shown in the Scheme 1B), ethyl violet (EV), CuSO$_4$, Co$_2$(SO$_4$)$_3$, 2,2'-azinobis(3-ethylbenzothiazolin-6-sulfonic acid) diammonium salt (ABTS), potassium ferrocyanide (K$_4$[Fe(CN)$_6$]) and potassium ferricyanide (K$_3$[Fe(CN)$_6$]) of analytical or better quality were commercially obtained. The buffer solution for photocurrent measurements is 0.1 M phosphate buffer solution (PBS, pH 7.4, KH$_2$PO$_4$-K$_2$HPO$_4$). Milli-Q ultrapure water (Millipore, $\geq$ 18 MΩ cm) was used in the experiments.

All electrochemical experiments were performed on a CHI660E electrochemical workstation (Shanghai Chenhua Instrument Co., Ltd.) equipped with a Xe lamp of 100 mW cm^{-2} (300 nm ~ 1100 nm). A conventional three-electrode electrolytic cell was used, and an FTO electrode with 0.25 cm^2 area and its modified electrodes served as the working electrode, a KCl-saturated calomel electrode (SCE) as the reference electrode, and a 3 mm diameter Pt disk electrode (area 0.0707 cm^2) as the counter electrode. A KSW-SX-4-10 muffle furnace (Beijing Yongguangming Medical Equipment Co., Ltd., China) was used for calcining to prepare CuCo$_2$O$_4$. The crystalline phase was measured by a Ultima IV (Rigaku Corporation, Japan) X-ray diffractometer (XRD). X-ray photoelectron spectroscopy (XPS) was performed on a Thermo Fisher X-ray photoelectron spectrometer. UV-vis diffuse reflectance spectra (DRS) was obtained on a Shimadzu UV-2600 UV-vis-NIR spectrophotometer (Shimadzu Co., Japan). Transmission electron microscopy (TEM) characterizations were performed on a JEM-2100 transmission electron microscope. Scanning electron microscopy (SEM) characterizations were performed on a TESCAN MIRAS scanning electron microscope,

which is equipped with an Oxford energy-dispersive X-ray spectroscopy (EDX) analysis detector for elemental analysis. Water contact angle was measured on a Germany-Dataphysics-OCA20 water contact angle tester. Fluorescence spectroscopy was obtained on a Hitachi F-7100 fluorescence spectrophotometer (Hitachi Co., Japan).

Preparation and characterization of some fluorescent materials

$NaYF_4$:Yb,Tm upconversion microrods were synthesized as reported previously[3], with a slight modification. First, 0.65 M NaOH was dissolved in 3.0 mL ultrapure water and mixed with 10 mL ethanol and 10 mL oleic acid under vigorous stirring. At the same time, 4.0 mL of 0.2 M $RECl_3$ (rare earth (RE) chlorides) mixture including $YbCl_3·6H_2O$, YCl_3, and $TmCl_3$ (molar ratio Y: Yb: Tm = 79.8: 20: 0.2) was added to 2.0 mL of 2.0 M aqueous NH_4F and stirred vigorously for 30 min. After that, the two resulting mixtures were transferred to a 50 mL Teflon autoclave and heated at 220 ^{o}C for 12 h. Finally, the obtained product ($NaYF_4$:Yb,Tm) was washed with ultrapure water and ethanol alternately by centrifugation, and dried at 80 ^{o}C. The prepared $NaYF_4$:Yb,Tm up-conversion nanomaterial was ultrasonically dissolved in ethanol to obtain 30 mg/mL $NaYF_4$:Yb,Tm suspension, then 6 μL $NaYF_4$:Yb,Tm suspension was cast-coated onto a clean FTO electrode and dried to obtain the $NaYF_4$:Yb,Tm/FTO electrode.

PPy was synthesized as reported previously[4]. Uniform PPy films were electropolymerized at -0.6 V~1.8 V in an aqueous electrolyte containing 0.1 M SDBS and 0.06 M pyrrole (Fig. S1).

CdS QDs were synthesized as reported previously with a slight modification[5]. 250 μL TGA was added to 50 mL of 10 mM aqueous $CdCl_2$ (initial concentrations were 72 mM for TGA and 10 mM for $CdCl_2$), and after adjusting the solution pH to pH 11 by adding 1.0 M aqueous NaOH, 0.1 M aqueous Na_2S was added drop by drop. The solution was aerated by N_2 throughout the whole process. After N_2 treatment for 4 h, QDs were precipitated by adding to acetone, centrifuged and redissolved in water at a concentration of 1 mg/mL. The synthesized CdS QDs were stored in refrigerator at 4 ^{o}C.

The preparations of $NaYF_4$:Yb,Tm microrods and CdS QDs were characterized by SEM, EDX and TEM. A typical rod-like topological structure is seen in Fig. S2, the signals of Na, Y, F, Yb and Tm elements confirm the presence of $NaYF_4$:Yb,Tm (Fig. S3). Moreover, the pure $NaYF_4$:Yb,Tm microrods with smooth surface can emit blue-violet light upon the NIR laser irradiation (inset in Fig. S2), indicating the successful preparation of the $NaYF_4$:Yb,Tm microrods. A typical TEM image of the synthesized CdS QDs is shown in Fig. S4, which exhibits uniform morphology with an average size of 7.8 nm in diameter.
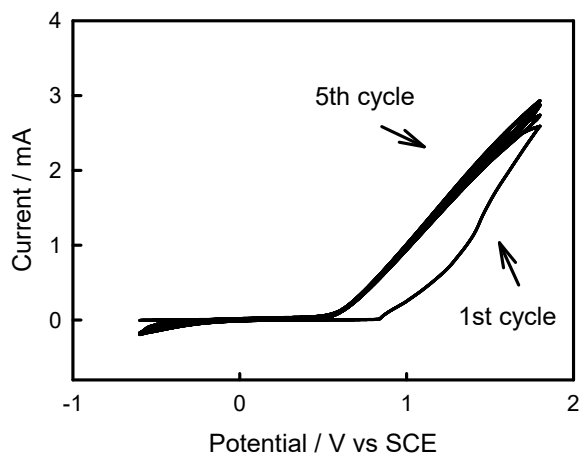
Fig. S1 CV curves of FTO electrode in 0.1 M SDBS and 0.06 M pyrrole solution. Scan rate: 50 mV s^{-1}. During the first positive scan, an oxidation current ramp appears at potentials positive of ca. 0.75 V. After the first CV cycle, a green-gray film can be observed on the FTO electrode surface, indicating the formation of PPy deposit. Since the electrode-deposited PPy film of appropriate thickness and the anodic formation of pyrrole oligomers (the greater conjugation degree of pyrrole oligomers makes them more easily oxidizable than pyrrole) near the electrode surface can facilitate the further oxidative polymerization of pyrrole, the oxidation current ramps during the subsequent CV cycles appear at more negative potentials and become larger than that during the first CV circle.
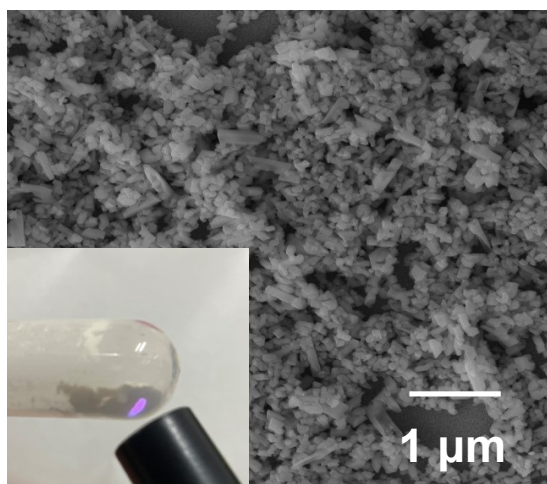
Fig. S2 SEM spectra of NaYF$_4$:Yb,Tm microrods, the inset shows the NaYF$_4$:Yb,Tm microrods can emit blue-violet light under the irradiation of 980 nm laser.
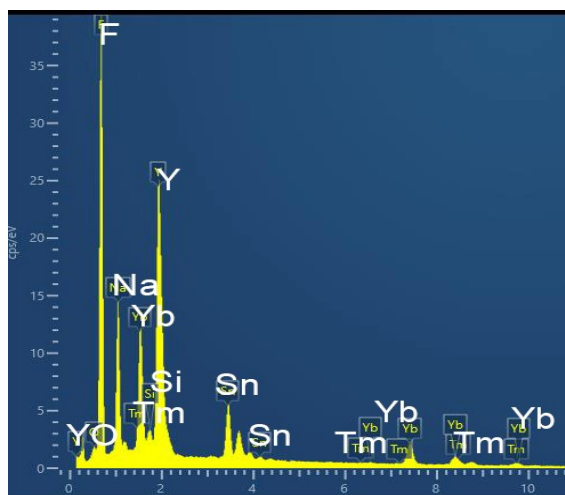
Fig. S3 EDX spectra of NaYF$_4$:Yb,Tm microrods.
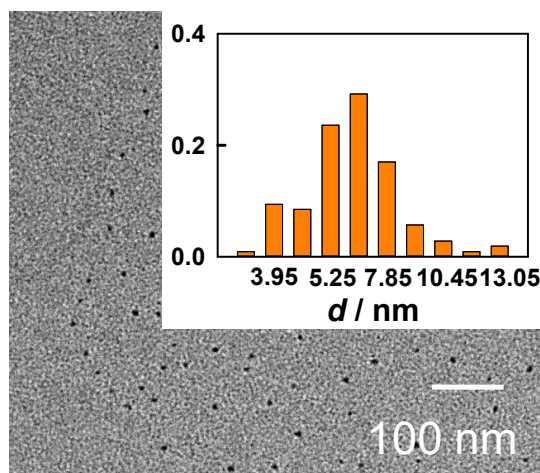
Fig. S4 TEM image of CdS QDs, the inset shows the size analysis by the Nano Measurer software.
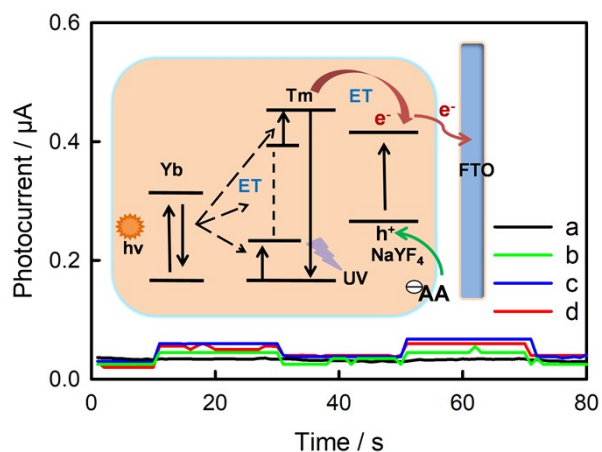
Fig. S5 Photocurrent responses of NaYF$_4$:Yb,Tm (a: FTO electrode with 0.1 M AA; b: NaYF$_4$:Yb,Tm/FTO electrode without AA; c: NaYF$_4$:Yb,Tm/FTO electrode with 0.1 M AA; d: NaYF$_4$:Yb,Tm/Au disk electrode with 0.1 M AA). The photocurrents were measured at 0 V vs SCE in 0.1 M PBS (pH 7.4); inset: schematic showing electron transfer of NaYF$_4$:Yb,Tm phosphor upon light excitation. Because NaYF$_4$:Yb,Tm has very poor conductivity and wide band gap [6], there are few photogenerated electrons excited to high energy levels, resulting in low photocurrent. Moreover, the electrons excited to a high energy level are extremely unstable, more energy can be released after they return to the ground state and recombine with holes, so the fluorescence intensity of rare earth fluorescent materials is generally stronger than that of semiconductors. After 0.1 M AA was added to PBS, it can be seen that the photocurrent increases significantly, indicating that the rare earth fluorescent material can generate photogenerated electrons and holes by charge separation under light excitation. There is also photocurrent on the NaYF$_4$:Yb,Tm/Au disk electrode in 0.1 M PBS containing 0.1 M AA, indicating that the photocurrent is not generated by the interaction between FTO and NaYF$_4$:Yb,Tm. The possible electron transfer mechanism is shown in the inset of Fig. S5.
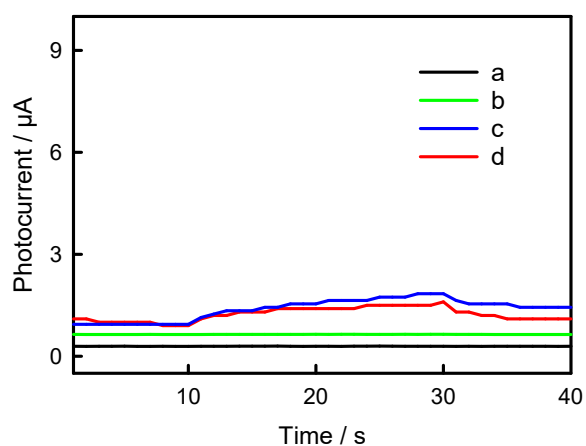
Fig. S6 Photocurrent responses of PPy (a: FTO electrode with 0.1 M AA; b: PPy/FTO electrode without AA; c: PPy/FTO electrode with 0.1 M AA; d: PPy/Au disk electrode with 0.1 M AA). The photocurrents were measured at 0 V vs SCE in 0.1 M PBS (pH 7.4). The PPy/FTO electrode has a weak photocurrent in PBS. After 0.1 M AA was added to PBS, the photocurrent increased to 450 nA. As demonstrated above, PPy can also be used to generate photogenerated electrons and holes by light excitation. There is a photocurrent on the PPy/Au disk electrode in the PBS containing AA, indicating that it is not the interaction between FTO and PPy that generated the photocurrent.
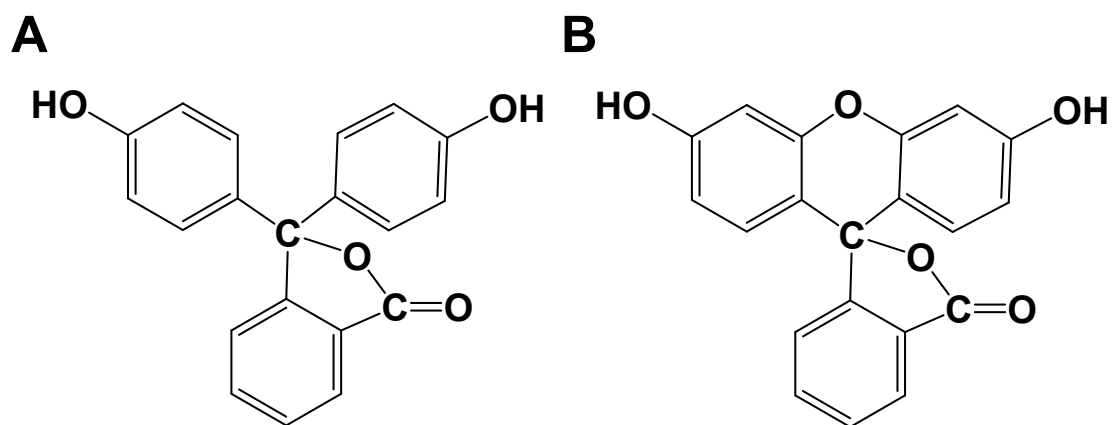
Fig. S7 Schematic diagram of molecular structures of phenolphthalein (A) and fluorescein (B).
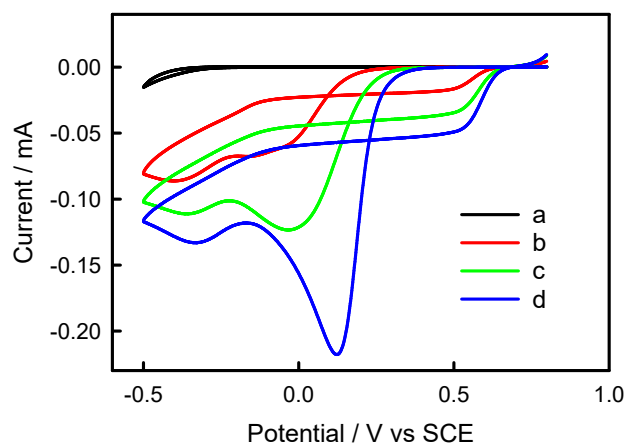
Fig. S8 CV curves of FTO electrode in 0.1 M aqueous KCl containing 0 (a), 0.1 (b), 0.5 (c), or 1 (d) mM $HAuCl_4$. Scan rate: 50 mV s^{-1}.
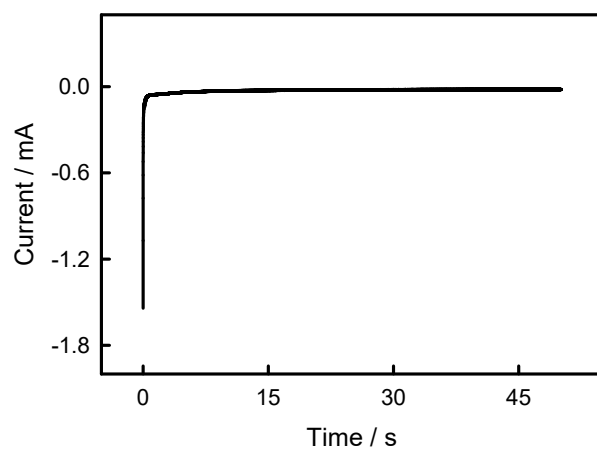
Fig. S9 The *i-t* curve of depositing AuNPs at -0.2 V for 50 s.
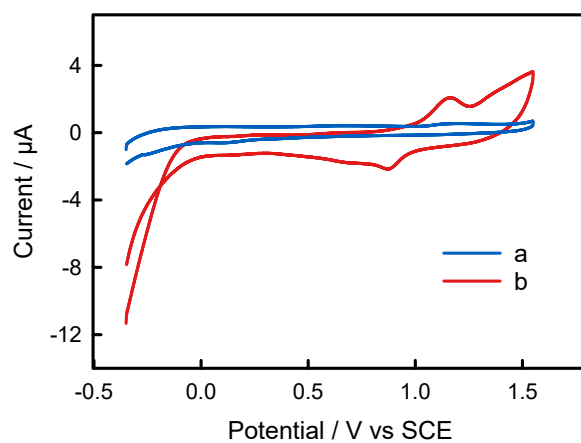
Fig. S10 CV curves of FTO (a) and AuNPs/FTO (b) electrodes in 0.5 M aqueous H_2SO_4. Scan rate: 50 mV s^{-1}.
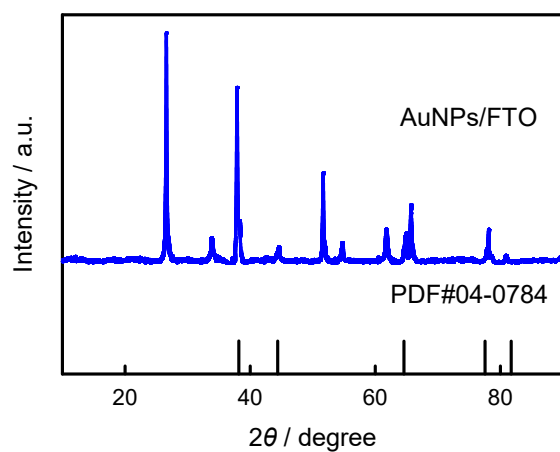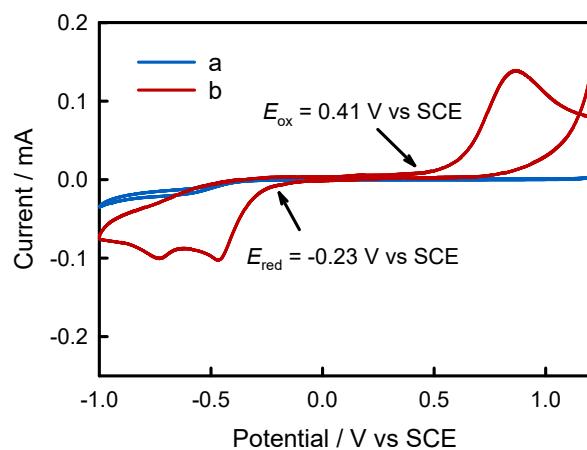
Fig. S11 XRD pattern of AuNPs/FTO electrode.

Material	E_{ox} (V vs SCE)	E_{red} (V vs SCE)	E_{HOMO} (eV)	E_{LUMO} (eV)	E_g (eV)
MV	0.41	-0.23	-4.85	-4.21	0.64

Fig. S12 CV curves of FTO electrode in 0.1 M PBS containing 0 (a), or 2 (b) mM MV. Scan rate: 50 mV s^{-1}. The electrochemical and PEC properties of MV can be derived from the CV curves.

E_g = 0.63 eV

E_{HOMO} = -4.88 eV E_{LUMO} = -4.25 eV
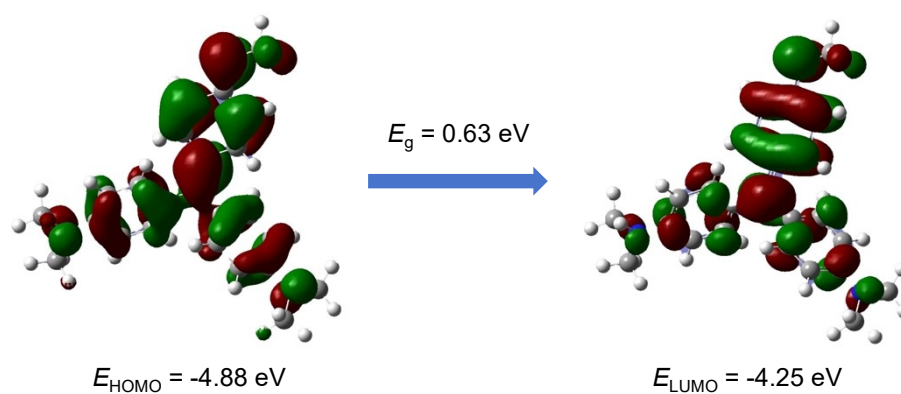
Fig. S13 HOMO and LUMO molecular orbital energy levels of MV. The colors represent the phases of the orbital wave function, the red is positive phase and the green is the opposite. The Gaussian's calculations were carried out in Gaussian (09W) program with Becke's three-parameter hybrid method using the Lee-Yang-Parr correlation functional (B3LYP) at 6-311+G(d,p) level[7, 8].
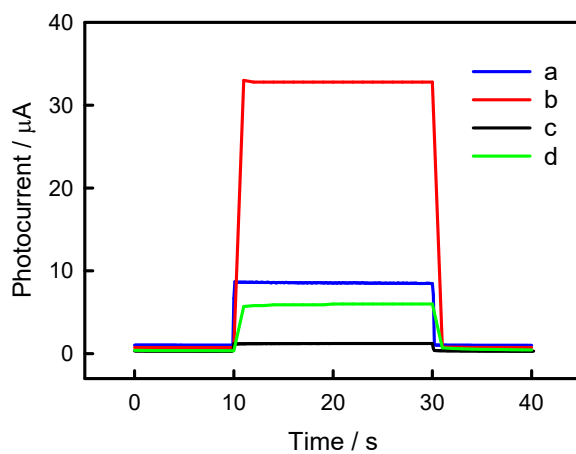
Fig. S14 Photocurrent responses of MV/AuNPs/FTO electrode of deposited AuNPs for 1250 s and absorbed MV for 125 min (a), (MV/AuNPs)$_{25}$/FTO electrode (b), NR/AuNPs/FTO electrode of deposited AuNPs for 1250 s and absorbed NR for 125 min (c), and (NR/AuNPs)$_{25}$/FTO electrode (d) in 0.1 M PBS (pH 7.4) containing 0.1 M AA at 0 V vs SCE.
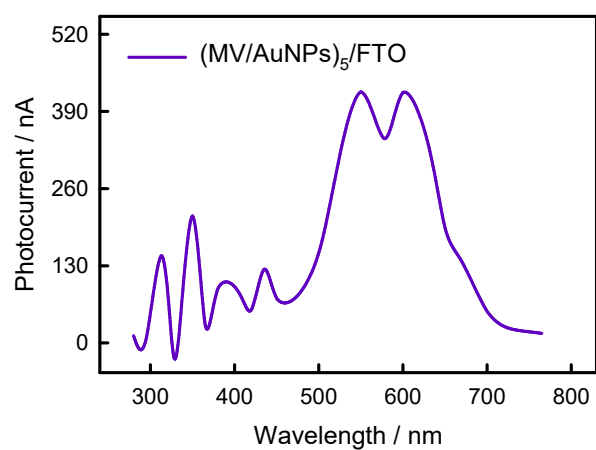
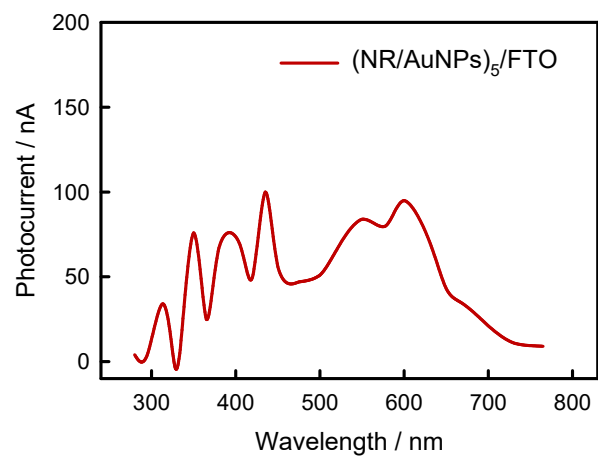**Fig. S15** Photocurrent-incident wavelength curve of (MV/AuNPs)$_5$/FTO electrode. The incident wavelength was determined by the optical filter.

Fig. S16 Photocurrent-incident wavelength curve of (NR/AuNPs)$_5$/FTO electrode. The incident wavelength was determined by the optical filter.
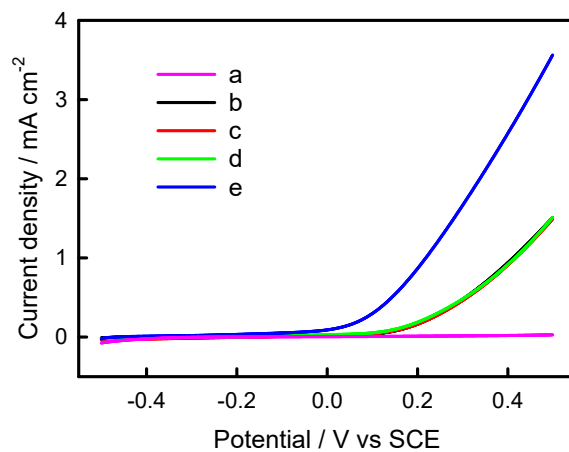
Fig. S17 LSV curves of (MV/AuNPs)$_{25}$/FTO electrode without AA (a), FTO (b), AuNPs/FTO (c), MV/AuNPs/FTO (d) and (MV/AuNPs)$_{25}$/FTO (e) electrodes with 0.1 M AA in 0.1 M PBS under illumination.
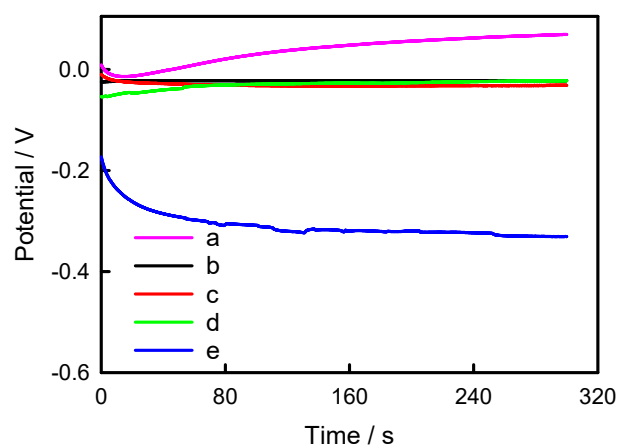
Fig. S18 Open circuit potential curves of (MV/AuNPs)$_{25}$/FTO electrode without AA (a), FTO (b), AuNPs/FTO (c), MV/AuNPs/FTO (d) and (MV/AuNPs)$_{25}$/FTO (e) electrodes with 0.1 M AA in 0.1 M PBS under illumination, and a Pt disk electrode as the reference electrode.
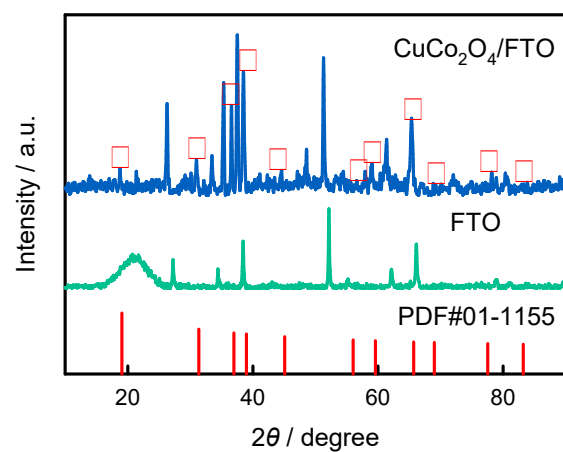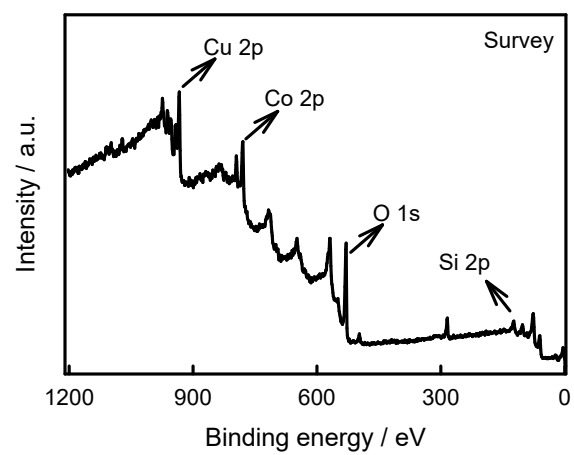
Fig. S19 XRD patterns of FTO and CuCo$_2$O$_4$/FTO.
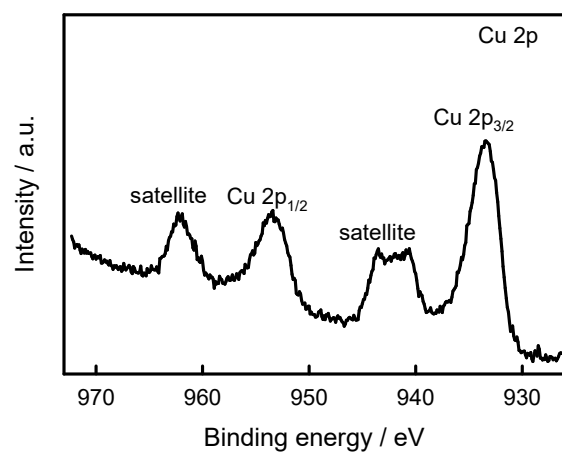
Fig. S20 XPS survey scan of CuCo$_2$O$_4$.

Fig. S21 Cu 2p XPS of CuCo$_2$O$_4$.
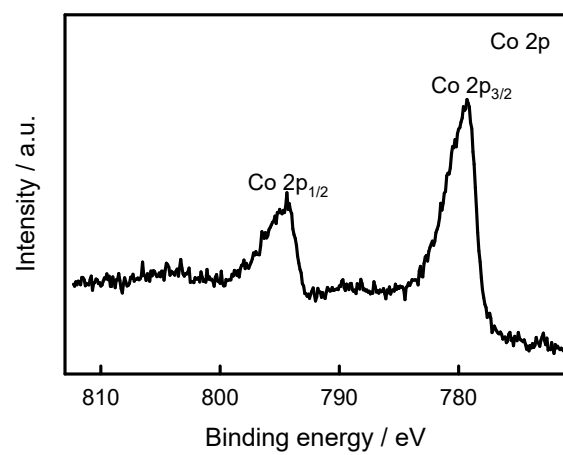
Fig. S22 Co 2p XPS of CuCo$_2$O$_4$.
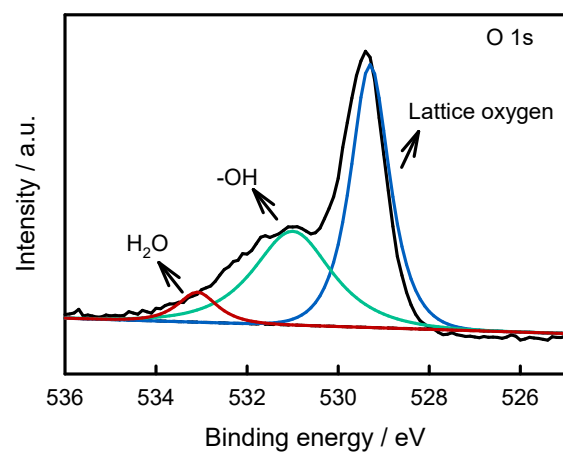
Fig. S23 O 1s XPS of $CuCo_2O_4$.
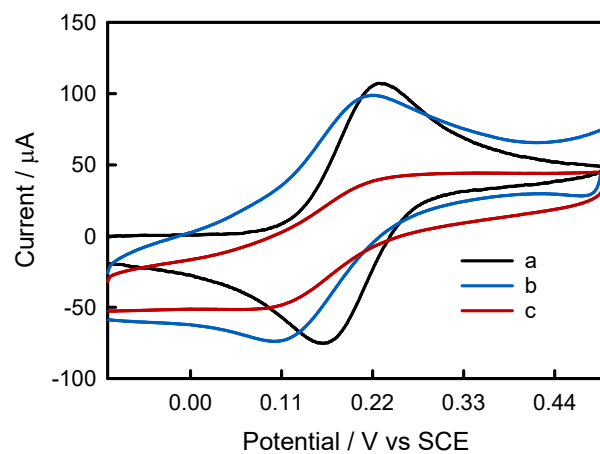
Fig. S24 CV curves of FTO (a), $CuCo_2O_4$/FTO (b), and BOD/$CuCo_2O_4$/FTO (c) electrodes in 0.01 M PBS containing 2.0 mM $K_4Fe(CN)_6$ and 0.1 M Na_2SO_4. Scan rate: 50 mV s^{-1}.
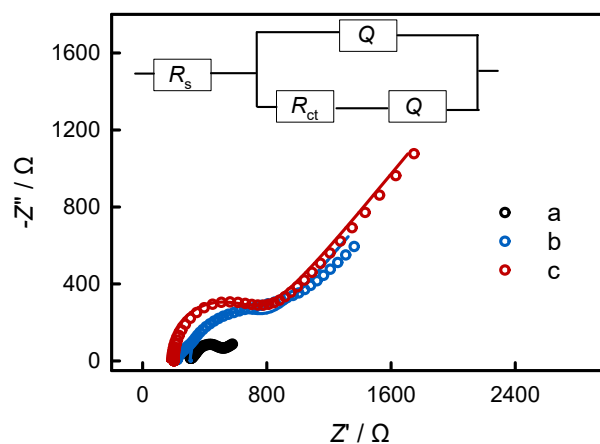
Fig. S25 EIS spectra of FTO (a), $CuCo_2O_4$/FTO (b), and BOD/$CuCo_2O_4$/FTO (c) electrodes in 0.01 M PBS containing 2.0 mM $K_4Fe(CN)_6$ and 0.1 M Na_2SO_4. EIS was measured after biased at 0.2 V for 200 s to ensure a 1:1 $Fe(CN)_6^{3-/4-}$ concentration ratio. Symbols in panel B: experimental; curves in panel B: fitted to the modified Randles equivalent circuit shown as the inset of panel B.
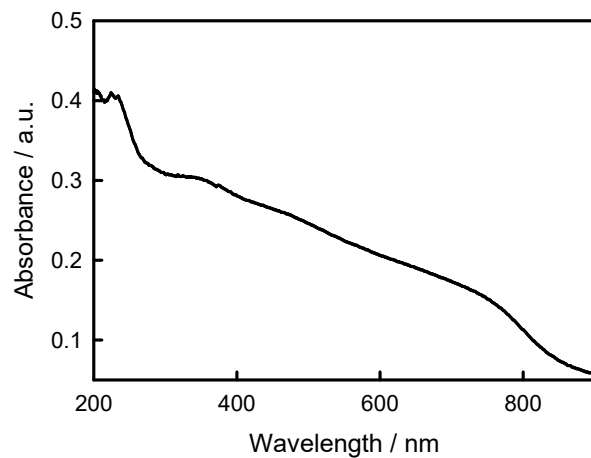
Fig. S26 UV-vis spectra of CuCo$_2$O$_4$.
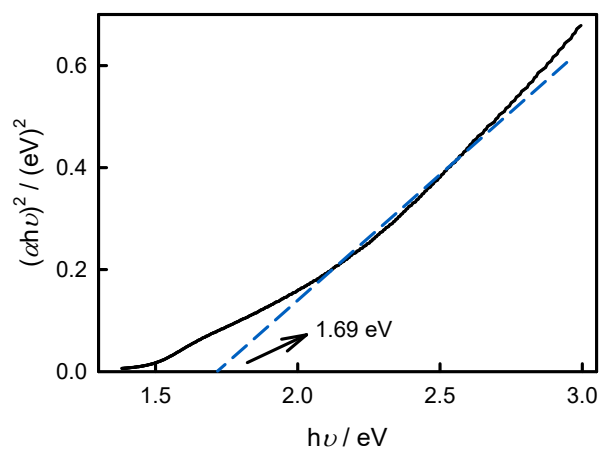
Fig. S27 Plots of $(\alpha h\upsilon)^2$ versus photon energy ($h\upsilon$) of $CuCo_2O_4$.

Fig. S28 Mott-Schottky curves of $CuCo_2O_4$ at 1 kHz in 0.1 M aqueous Na_2SO_4.
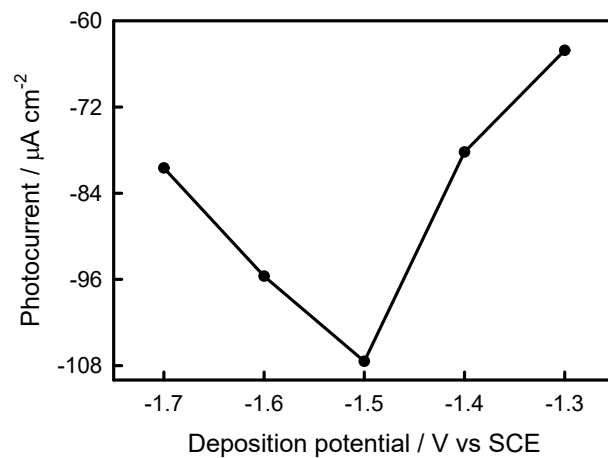
Fig. S29 Effects of different deposition potentials on the photocurrent of CuCo$_2$O$_4$/FTO electrode in oxygen-saturated 0.1 M PBS (pH 7.4) at 0 V vs SCE.
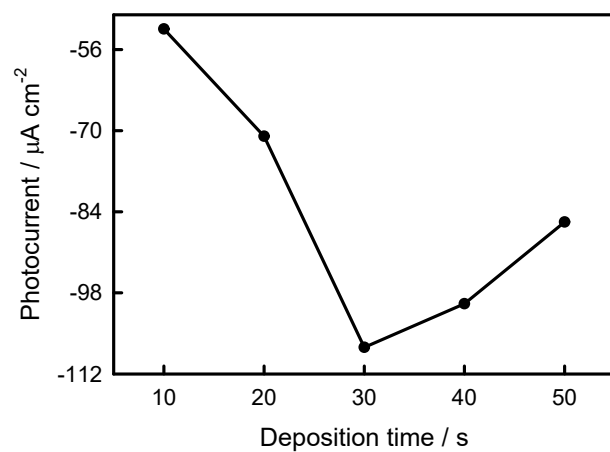
Fig. S30 Effects of different deposition times on the photocurrent of CuCo$_2$O$_4$/FTO electrode in oxygen-saturated 0.1 M PBS (pH 7.4) at 0 V vs SCE.

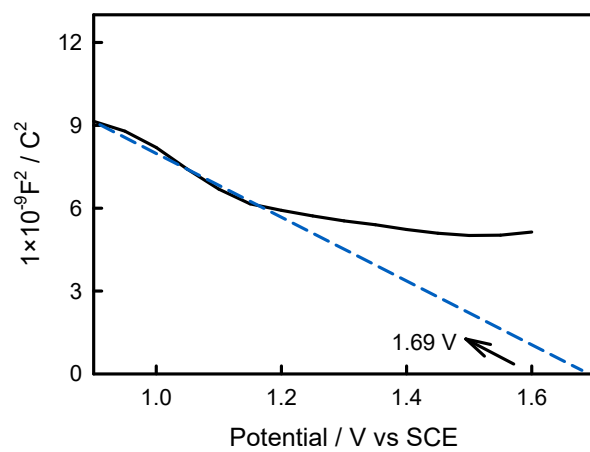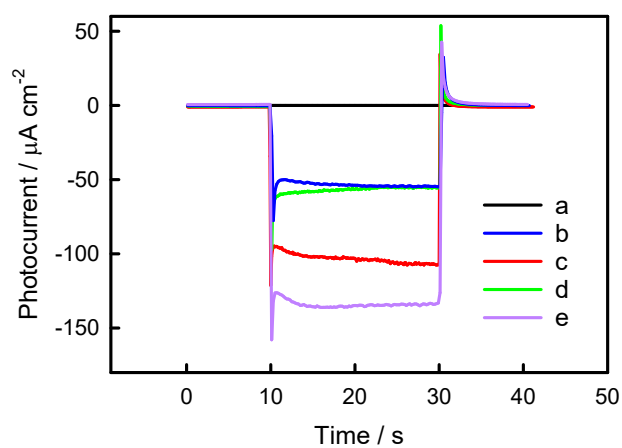**Fig. S31** Photocurrent responses of FTO (a), CuCo$_2$O$_4$/FTO (b) electrodes in 0.1 M PBS, and CuCo$_2$O$_4$/FTO (c), BOD/CuCo$_2$O$_4$/FTO (d) electrodes in oxygen-saturated 0.1 M PBS, and BOD/CuCo$_2$O$_4$/FTO (e) electrode in oxygen-saturated 0.1 M PBS (pH 7.4) containing 0.5 mM ABTS at 0 V vs SCE.

Table S1 Performance comparison of this PEBFC with other EBFCs and dye-sensitization based PEBFCs.

Cell	Anode	Cathode	V_{oc} (V)	P_{max} ($\mu W\ cm^{-2}$)	FF	η	Ref.
EBFC	Glucose oxidase (GOD)/ poly(ethylene glycol) diglycidyl ether + (PAA-PVI-[Os(dmo-bpy)$_2$Cl]$^{+/2+}$) + glucose	BOD + PAA-PVI-[Os(dCl-bpy)$_2$Cl]$^{+/2+}$ + O$_2$	0.38	11.2	-	-	9
EBFC	GOD/polystyrene-*block*-poly(4-vinylpyrdine) (PS-*b*-P4VP) + glucose	PS-*b*-P4VP/laccase + O$_2$	0.42	3.49	-	-	10
EBFC	GOD/graphene-coated single-wall carbon nanotube (SWCNT) + glucose	BOD/graphene-coated SWCNT + O$_2$	0.22	3.6	-	-	11
EBFC	*Pediococcus sp.* lactate oxidase/Os polymer/nanoporous gold (NPG) + lactic acid	BOD/diazonium-modified NPG + O$_2$	0.455 ± 0.021	2.4 ± 0.2	-	-	12
PEBFC	Multiwalled carbon nanotubes (MWCNT)/g-C$_3$N$_4$/Ru-complex/glucose dehydrogenase (GDH) + glucose	MWCNT/BOD + O$_2$	0.64	28.5	-	-	13
PEBFC	GDH/meso-tetra(p-hydroxyphenyl)porphine/TiO$_2$ + glucose	Pt + O$_2$	0.50	15.9	0.41	0.016 %	14
	GDH/ tetrakis(4-carboxyphenyl)porphyrin/TiO$_2$ + glucose		0.74	33.9	0.19	1.46 %	
PEBFC	GDH/tetrakis (4-carboxyphenyl) porphyrin (TCPP)/mesoporous TiO$_2$ nanocrystal + glucose	Pt + O$_2$	0.74	0.67	0.43	-	15
PEBFC	Chlorin-e6/TiO$_2$ + glucose	BOD and ABTS-modified carbon-based electrode + O$_2$	0.53	1.7	0.36	0.0017 %	16
PEBFC	GDH/TCPP/TiO$_2$ + glucose	Pt + O$_2$	0.57	0.9	0.47	-	17
PEBFC	GDH/porphyrin/SnO$_2$ + glucose	Hg/Hg$_2$SO$_4$ + O$_2$	0.75	9.5	0.42	-	18
PEBFC	PSII/Os polymer/microporous carbonaceous material + glucose	BOD/MWCNT + O$_2$	0.531	-	-	-	19
PEBFC	(MV/AuNPs)$_{25}$/FTO + AA	BOD/CuCo$_2$O$_4$/ FTO + ABTS+ O$_2$	0.73	14.1	0.25	0.014%	This work

References

1. M. A. Omary and H. H. Patterson, in *Encyclopedia of Spectroscopy and Spectrometry*, ed. J. C. Lindon, Elsevier, Oxford, 1999, pp. 1186-1207.

2. B. Valeur and M. N. Berberan-Santos, *Molecular fluorescence: principles and applications*, John Wiley & Sons, 2013.

3. Z. L. Qiu, J. Shu and D. P. Tang, *Anal Chem*, 2018, **90**, 1021-1028.

4. S. Kim, L. K. Jang, M. Jang, S. Lee, J. G. Hardy and J. Y. Lee, *ACS Appl Mater Interfaces*, 2018, **10**, 33032-33042.

5. C. L. Sun, Y. R. Shen, Y. Zhang, Y. Du, Y. Y. Peng and Q. J. Xie, *Talanta*, 2023, **253**, 123882.

6. Y. Zhai, D. L. Liu, Y. D. Jiang, X. Chen, L. Shao, J. Li, K. Sheng, X. R. Zhang and H. W. Song, *Sens Actuator B-Chem*, 2019, **286**, 468-475.

7. A. D. Becke, *J Chem Phys*, 1993, **98**, 5648-5652.

8. Y. C. Gao, N. Yao, X. Chen, L. Yu, R. Zhang and Q. Zhang, *J Am Chem Soc*, 2023, **145**, 23764-23770.

9. W. Y. Jeon, J. H. Lee, K. Dasbnyam, Y. B. Choi, T. H. Kim, H. H. Lee, H. W. Kim and H. H. Kim, *Sci Rep-UK*, 2019, **9**.

10. Y. Zang, H. M. Zhu and H. G. Xue, *Electrochim Acta*, 2018, **259**, 676-684.

11. A. S. Campbell, M. V. Jose, S. Marx, S. Cornelius, R. R. Koepsel, M. F. Islam and A. J. Russell, *RSC Adv*, 2016, **6**, 10150-10158.

12. X. X. Xiao, T. Siepenkoetter, P. O. Conghaile, D. Leech and E. Magner, *ACS Appl Mater Interfaces*, 2018, **10**, 7107-7116.

13. B. Cakiroglu, J. Chauvin, A. Le Goff, K. Gorgy, M. Ozacar and M. Holzinger, *Biosens Bioelectron*, 2020, **169**.

14. J. Yang, B. Wang, Y. P. Miao and B. Sun, *J Inorg Organomet P*, 2014, **24**, 371-380.

15. C. P. Xiao, L. L. Ji, D. H. Li, L. Q. Wang and J. Yang, *J Chem Res*, 2021, **45**, 374-379.

16. Y. Amao, Y. Sakai and Y. Teshima, *Res Chem Intermediat*, 2016, **42**, 7761-7770.

17. C. C. Tang, B. Wang, W. Xing, D. H. Hu and J. Yang, *J Iran Chem Soc*, 2016, **13**, 261-266.

18. A. Brune, G. Jeong, P. A. Liddell, T. Sotomura, T. A. Moore, A. L. Moore and D. Gust, *Langmuir*, 2004, **20**, 8366-8371.

19. B. Çakıroğlu, N. Jabiyeva and M. Holzinger, *Biosens Bioelectron*, 2023, **226**, 115133.